Mechano-sensitization of mammalian neuronal networks through expression of the bacterial mechanosensitive MscL channel

Alessandro Soloperto[1*], Anna Boccaccio[2], Andrea Contestabile[1], Monica Moroni[3], Grace I. Hallinan[5], Gemma Palazzolo[1], John Chad[5], Katrin Deinhardt[5], Dario Carugo[4] and Francesco Difato[1*]

[1] Neuroscience and Brain Technologies Dept., Istituto Italiano di Tecnologia, Genoa, Italy.

[2] Institute of Biophysics, National Research Council of Italy, Genoa, Italy.

[3] Center for Neuroscience and Cognitive Systems, Istituto Italiano di Tecnologia, Rovereto, Italy.

[4] Faculty of Engineering and the Environment, University of Southampton, Southampton, United Kingdom.

[5] Biological Sciences and Institute for Life Sciences, University of Southampton, Southampton, United Kingdom.

*corresponding authors e-mail: alessandro.soloperto@iit.it and francesco.difato@iit.it

Summary statement

We report the development and characterization of mechano-sensitized neuronal networks through the heterologous expression of an engineered bacterial large conductance mechanosensitive ion channel (MscL).

Abstract

Development of remote stimulation techniques for neuronal tissues represents a challenging goal. Among the potential methods, mechanical stimuli are the most promising vector to convey information non-invasively into intact brain tissue. In this context, selective mechano-sensitization of neuronal circuits would pave the way to develop a new cell-type specific stimulation approach. We report here for the first time the development and characterization of mechano-sensitized neuronal networks through the heterologous expression of an engineered bacterial large conductance mechanosensitive ion channel (MscL). The neuronal functional expression of the MscL channel was validated through patch-clamp recordings upon application of calibrated suction pressures. Moreover, we verified the effective development of in-vitro neuronal networks expressing the engineered MscL channel in terms of cell survival, number of synaptic puncta, and spontaneous network activity. The pure mechanosensitivity of the engineered MscL channel, with its wide genetic modification library, may represent a versatile tool to further develop a mechano-genetic approach.

Keywords

Nanopore engineering/Neuronal mechano-sensitization/Mechanobiology/MscL/Exclusively mechanosensitive ion channel

JCS Advance Online Article. Posted on 29 January 2018

Introduction

Neuronal stimulation techniques are essential tools for investigating brain functions and treating neurological diseases (Rogan and Roth, 2011). Current understanding of the mechanisms regulating the physiology of the central nervous system is still limited, thus novel approaches to manipulate the activity of neuronal circuits are required to gain further insights into brain physiology (Panzeri et al., 2017), and to allow the design of alternative and more effective strategies to treat neurological disorders. Established approaches for interrogating and dissecting neuronal circuits' function often involve the use of chemical, electrical and/or optical stimulation. Although these methods have allowed important advancements in the field of neuroscience, they all present significant limitations. Chemical stimulation suffers from poor spatial selectivity and low pharmacokinetic control. The development of a chemogenetic actuator, based on G protein-coupled receptors activated by ad hoc designed synthetic small molecules (DREADDs), provided a cell-type specificity to the chemical stimulation approach (Armbruster et al., 2007), overcoming the selectivity issues. However, DREADD technology still provides a low temporal resolution, in the range of minutes-hours, in controlling the neuronal activity (Whissell et al., 2016).

On the contrary, electrical and optical stimulation are paving the way for the development of neuro-prosthetic systems working at high temporal bandwidth and down to single-cell resolution (Cash and Hochberg, 2015). Their clinical translation is however hindered by several practical limitations, including the high degree of surgical complexity and the invasiveness associated with the implantation of stimulation devices (i.e. electrodes and optical fibers). Moreover, related side effects such as glial scar formation, tissue inflammation, immune responses, and performance deterioration of the implanted probes, significantly limit the treatment lifetime (Grill et al., 2009) and complicate the analysis.

Optical stimulation currently represents the most effective strategy for studying the physiology of neuronal circuits as it provides the benefit of contact-free focal stimulation of sub-cellular compartments, or cell type-specific stimulation within a tissue through the selective genetic expression of light-sensitive ion channels (Beltramo et al., 2013).

Drawbacks of this approach are limited penetration into the tissue and phototoxicity that accompanies repeated stimulation. Moreover, both chemogenetic and optogenetic manipulations require genetic modification of the tissue (Jorfi et al., 2015), typically via viral vectors, which limits translation to clinical application. Therefore, within a clinical environment, implantation of electrodes remain the preferred choice for evaluation of rehabilitation protocols.

The ideal brain stimulation technology should thus avoid implantation of devices, achieving wireless remote-modulation of neuronal circuits' activity. Moreover, it should be safe in the long-term, and provide high spatial and temporal control of the stimulus (Tay et al., 2016).

Alternative approaches to the surgical implantation of probes include transcranial electrical, thermal, magnetic, and ultrasound stimulation (Fregni and Pascual-Leone, 2007). While transcranial electrical (Grossman et al., 2017) and thermal (Wang and Guo, 2016) stimulation suffer from poor spatial resolution, magnetic and ultrasound (US) fields efficiently propagate across the intact skull bone, and they could be focused in small focal volumes at clinically relevant tissue depths (Tyler et al., 2008). In particular, US fields provide deeper penetration and improved spatial focusing within dense tissue. Moreover, the use of US pressure fields as a mean for modulating neuronal activity is attracting considerable interest since US sources can be miniaturized (Li et al., 2009) and thus, portable and implantation-free US stimulation devices could be easily designed. Moreover, the safety of US waves in biomedical applications has been widely demonstrated, and it is extensively utilized in the clinic for biomedical imaging, rehabilitation physiotherapy, thrombolysis, and tumor ablation (Krishna et al., 2017). However, the application of low-intensity US fields for delicate and reversible alterations in cells and tissues is still in its infancy, due to the limited understanding of the biophysical mechanisms involved (Dalecki, 2004; Tyler, 2011). A similar debate has emerged on the use of magnetic fields, and an unifying theoretical and experimental framework for these forms of stimulation has not been established yet (Meister, 2016). Several models for US-mediated bioeffects have been proposed, including those based on localized heating, acoustic streaming, intramembrane cavitation (Krasovitski et al., 2011), membrane leaflet separation, and modulation of mechanosensitive (MS) ion channels (Tyler, 2011). It is worth noting that direct experimental evidence of US pressure waves affecting the activity of mechanosensitive ion channels has been provided only recently (Kubanek et al., 2016), thus corroborating the hypothesis that low-intensity US can potentially modulate cellular mechanotransduction pathways (Hertzberg et al., 2010).
In this regard, advances in mechanobiology have led to the discovery, design, and application of cellular transduction pathways, as demonstrated in recent studies reporting on the use of mechanosensitive ion channels for triggering a cellular response, using either magnetic (Wheeler et al., 2016) or ultrasound-based (Ibsen et al., 2015) mechanical stimulation. The extraordinary achievements of these studies have laid the foundation of two new research areas, referred to as magnetogenetics and sonogenetics (in addition to the already established optogenetics and chemogenetics). However, most mechanosensitive ion channels, such as TRPV4, display an intrinsic sensitivity to other endogenous stimuli (i.e., voltage, heat, pH, etc.), thus preventing isolated investigation of mechanosensitive responses. Notably, the aforementioned study suggested that the

overexpression of non-exclusively MS ion channels may compromise the physiology of neuronal circuits (Wheeler et al., 2016); therefore, molecular engineering of these channels is required to render them insensitive to other forms of stimuli.

Mechanotransduction is regarded as one of the evolutionarily oldest signal transduction pathway, and MS channels are one of the most important cellular element for sensing and transducing mechanical forces (Hamill and Martinac, 2001; Martinac, 2014). However, few MS ion channels behave as exclusively mechanosensitive elements, and this list has only recently been updated to include the first mammalian exclusively MS ion channel: the Piezo channel (Coste et al., 2012). Indeed, the first identified exclusively MS ion channel was the bacterial protein known as large conductance mechanosensitive ion channel (MscL) (Kung et al., 2010; Sukharev et al., 1994). MscL is a homopentameric pore-forming membrane protein which acts as a release valve of cytoplasmic osmolytes when the membrane tension increases (Sawada et al., 2012). The ability to easily isolate large amounts of the MscL channel from many bacterial strains, and to reconstitute it in a cell-free system, has allowed detailed characterization of its structure and biophysical properties (Kloda et al., 2008; Martinac et al., 2014; Sukharev et al., 1997). This has facilitated the design and development of new genetically modified variants of the MscL (Maurer and Dougherty, 2003) for potential exploitation in medical and biotechnological applications. Currently, MscL is the standard biophysical model for studying MS channels (Iscla and Blount, 2012), and its large pore diameter of about 30 Å is considered an ideal feature for developing triggered nano-valves for controlled drug release (Doerner et al., 2012; Iscla et al., 2013). Notably, thanks to its extensive characterization, the MscL channel also represents a malleable nano-tool that could be engineered with respect to channel sensitivity (Yoshimura et al., 1999), conductance (Yang et al., 2012) and gating mechanism (Kocer, 2005).

In this paper we demonstrate the use of the exclusively MS MscL channel to create mechano-sensitized mammalian neuronal networks, and thus provide a suitable model to study and further develop the sonogenetic paradigm. We generated an engineered MscL construct for mammalian expression that efficiently localizes to the plasma membrane, and thus demonstrate the first functional expression of MscL channels in primary mammalian neuronal cultures. Moreover, we performed structural and functional characterization of neuronal cells expressing the MscL channel, at both single-cell and network levels. Importantly, we show that the functional expression of the engineered MscL channel induces neuronal sensitivity to mechanical stimulation without affecting the physiological development of the neuronal network. Overall, our data demonstrate the development of a mechano-sensitized neuronal network model to reliably investigate, test and calibrate the stimulation of excitable circuits through remotely-generated mechanical energy fields.

Results

Membrane targeting of the bacterial MscL ion channel in primary neuronal cultures.

In the present work, we established an experimental model of mechano-sensitized neuronal networks. We designed a mammalian expression vector encoding for the bacterial MscL ion channel (from *Escherichia coli* bacterial strain) fused to tdTomato fluorescent protein under the control of the neuronal-specific synapsin 1 promoter (MscL-v.1 in Fig. 1A).

However, a first functional assessment of MscL-tdTomato expression in primary neuronal cells revealed a significant impairment in the delivery of the heterologous protein to the plasma membrane. In fact, transfected neurons showed large intracellular accumulation and clustering of MscL-tdTomato that consequently resulted in low membrane expression (Fig. 1B, left column panels). We reasoned that the accumulation and clustering of MscL could likely depend on the lack of a mammalian-specific export signal that prevents protein retention in the endoplasmic reticulum (ER) (Li et al., 2000). Following previous studies that optimized the mammalian expression of optogenetic actuators (Gradinaru et al., 2008), we fused the export signal of Kir2.1 ion channel (MscL-v.2 in Fig. 1A) to the cytoplasmic C-terminus of our MscL-tdTomato protein. The Kir2.1 ER export sequence (FCYENEV) has been extensively studied, and it is known to mediate efficient trafficking and surface expression of the channel (Hofherr, 2005; Stockklausner et al., 2001). Moreover, Kir channel monomers present structural similarities (e.g. two transmembrane domains, cytoplasmic N- and C-terminus) with MscL monomers, likely suggesting a similar pathway in protein trafficking.

In order to assess the membrane localization of naïve MscL (MscL-v1) versus MscL-v.2 bearing the ER export signal, we co-transfected primary neuronal cell cultures with two plasmids: the tdTomato-tagged MscL (either MscL-v1 or Mscl-v2) and a membrane-targeted myristoylated GFP (myr-GFP). Confocal microscopy examination confirmed enhanced localization of the MscL-v.2 channel along the neuronal membrane (Fig. 1B, right column panels), presumably due to prevention of ER retention and aggregation. In fact, a representative fluorescence intensity profile (along a cross-section line from the center of the cell soma to the plasma membrane; Fig. 1C) of tdTomato-tagged MscL-v.1 (red line), together with the membrane-targeted GFP (green line), shows prominent intracellular localization of MscL-v.1, resulting in the absence of fluorescent co-localization with myr-GFP at the plasma membrane of the cell (vertical dashed lines). Conversely, tdTomato-tagged MscL-v.2 fluorescence largely co-localized with myr-GFP, indicating efficient plasma membrane delivery of the channel. Quantitative evaluation of the co-localization index of the two fluorescent proteins by Pearson correlation analysis showed a coefficient of 0.54±0.02 (n= 11) for the MscL-v.1 construct,

indicating no significant co-dependency between the two fluorescence signals, and a coefficient of 0.86±0.04 (n= 8) for the MscL-v.2 construct, which confirmed a successful increase in membrane expression of the engineered MscL ion channels (Fig. 1D).

Importantly, neurons expressing the MscL-v.2 protein showed a good expression level of the channel even at later days in culture (20 DIV), both in the soma, neurites, and spine-like structures, thus indicating that MscL-v.2 expression was well-tolerated in primary neurons (Fig. 2A; Fig. S1A). However, considering that an enhanced mechanosensitivity could affect neurite growth and branching during network development, we compared the complexity of the dendritic tree of neurons expressing the MscL-v.2 channel with respect to neurons expressing only the membrane-targeted GFP.

Furthermore, this analysis was carried out on both wild type (WT) MscL-v.2 channel and on a gain of function MscL variant bearing a serine to glycine substitution at position 22 (G22S MscL-v.2), which leads to a lower activation pressure threshold (Yoshimura et al., 1999). As illustrated in Fig. 2B and 2C, the morphology of neurons expressing either WT or G22S MscL-v.2 channel did not show any significant alteration in terms of neurite length and number of primary branches, when compared to the control neurons expressing only the myr-GFP. In addition, the complexity of the overall neuronal arborization was unaltered, as determined by the similar number of endpoints between neurons expressing the myr-GFP or neurons expressing one of the two versions of the MscL-v.2 channel (Fig. S1B and S1C). Staining of the synaptic boutons further confirmed the unaltered number of endpoints (see section: Functional characterization of mechano-sensitized neuronal networks, Fig. 4A).

Electrophysiological characterization of the engineered MscL channel functionality.

After confirming the efficient and well-tolerated expression of the MscL-v.2 channel (hence forward indicated as eMscL), we verified its functionality and mechanosensitivity through pressure/voltage-clamp recordings in cell-attached configuration. All recordings were performed by patching primary rat cortical neurons between 12-14 DIV (Fig. 3A). Negative pressure was manually applied and set to 150 mmHg, through a custom pressure-clamp system (see methods section: Patch-clamp recordings and pressure-clamp system), in order to stretch the cell membrane into the patch pipette and thus trigger the gating of the eMscL channel (Fig. 3B). Both WT and G22S eMscL showed different responses in terms of current amplitude when mechanically stimulated (Fig. 3C and 3E; Fig. S2), indicating the possible presence of distinct sub-conductance states of the channel, as described previously (Cox et al., 2016). Accordingly, we classified the responses into two groups: a partial response, characterized by bursts of small current events, and a full response, characterized by higher current amplitude with smaller noise and a sharp and steep closure when the pressure stimulus is

removed. The partial response was often observed during the first cycles of stimulation, and was subsequently replaced by a full response. In Figures 3C and 3E, we present representative traces of the induced ion currents upon stimulation of either WT or G22S eMscL channel (blue and green color traces, respectively). Control experiments were on neurons expressing only the tdTomato fluorescence protein, since a specific MscL inhibitor is not available yet. In contrast, in control neurons (n= 74 stimulation runs, on n= 15 cells) stretch-induced currents were absent (Fig. 3D). This data indicates that the currents recorded from eMscL expressing neurons were due to the specific activity of the engineered channel rather than endogenous expression of other mechanically-gated channels or Piezo family channels (Tay and Di Carlo, 2017). Finally, we quantified the pressure activation threshold for both WT and G22S eMscL channels (Fig. 3F). Surprisingly, the partial response showed a similar activation threshold for both MscL variants (WT eMscL: 145±0.98 mmHg, n= 72 stimulation runs, on n= 19 cells; G22S eMscL: 142.50±0.91 mmHg, n= 111 stimulation runs, on n= 24 cells). On the contrary, the full response showed a predictable lower activation threshold for the G22S mutant (75.78±3.60 mmHg, n= 67 stimulation runs, on n= 17 cells) when compared to the WT (130±2.36 mmHg, n= 48, on n= 10 cells). Indeed, the partial response may well be due to the interaction of the cell cytoskeleton with the plasma membrane, which counteracts the membrane stretch and the complete MscL opening. Likewise, the similar activation threshold measured for the partial response in both WT and G22S expressing cells may reflect the membrane resistance to stretch (Martinac, 2014).

In this regard, for a better understanding of the stretch strain provided on the plasma membrane, we also estimated the bilayer tension corresponding to the measured activation pressure thresholds for the WT and G22S channels (see methods section: Estimating the applied membrane tension).

Under our experimental conditions, taking in account two values of adhesion energies of the cell membrane to the glass pipette (i.e., 3.7 $mN \cdot m^{-1}$ in case of homogenous phospholipid membrane (Ursell et al., 2011), and 1.6 $mN \cdot m^{-1}$ in the case of brain cell membrane (Suchyna et al., 2009), we estimated a tension range of 11.6÷13.7 $mN \cdot m^{-1}$ at a negative pressure of about 150 mmHg; and a tension range of 6.2÷8.3 $mN \cdot m^{-1}$ at a negative pressure of 70 mmHg. Both ranges are in line with those previously described in literature for the WT and the G22S MscL channels (Rosholm et al., 2017).

Once the functional expression of the MscL channels in neuronal cells was confirmed, we developed an adeno associated virus (AAV) expressing the G22S eMscL to allow higher expression rates, and we carried out the patch-clamp experiments again, in order to validate the MscL-induced mechano-sensitization of neurons, when the virally encoded G22S eMscL construct is used.

Also in this case, we measured in cell-attached configuration the activation pressure thresholds of the

current for the partial and full responses (141±0.48 mmHg, N= 65 stimulation trials and 70±0.72 mmHg, N= 21 stimulation trials, respectively), and we confirmed the previously measured values for the not virally encoded G22S eMscL construct (Fig. 3F).

Moreover, we measured the activation threshold of the G22S eMscL-induced currents in excised membrane patch (Fig. S3), showing that the activation pressure (67±0.14 mmHg, N= 69 stimulation trials) was similar to the value found for the G22S full response in cell-attached configuration (Fig. 3F). Taking in account these new set of data, we also confirmed our hypothesis that the partial response, recorded in cell-attached configuration, reflected the action of the cell cytoskeleton counteracting the cell membrane stretch. Indeed, it is important to take in account that even if MscL channels are gated directly by tension along the plasma membrane, the mechanical properties of the membrane could be altered by cytoskeletal proteins and other scaffold proteins linking the cell to the extracellular matrix (Cox et al., 2016).

Next, we performed the same set of experiments on neurons expressing eMscL channels at later DIV (15-18 DIV), when the cultured neuronal networks is matured and neurons are able to generate spiking activity (Soloperto et al., 2016), in order to investigate the potential for the eMscL channel to stimulate the generation of neuronal action potentials (APs). In Figure 3G, we illustrate a representative trace recorded by patching a neuron expressing G22S eMscL channel upon application of a negative pressure ramp. The mechanical stimulation was applied on the same cell patch, before and after application of 1 µM tetrodotoxin (TTX, indicated by dark and light blue traces respectively), which blocks the voltage-gated Na^+ channel and the generation of spontaneous APs. Induced-spike activity was present in neuron expressing both eMscL variants, and it was absent upon treatment with 1 µM TTX, while the currents induced by eMscL opening were preserved. Interestingly, only channel currents with amplitude below 50 pA were associated with the generation of action potentials in both WT and G22S eMscL-expressing neurons (dashed black box in Fig. 3G; WT eMscL: 5 out of 9 cells; G22S eMscL: 9 out of 17 cells). In contrast, eMscL-induced currents with higher amplitudes failed to trigger APs, presumably due to a massive membrane depolarization. Furthermore, we could occasionally detect an increase of the neuronal spiking activity upon mechanical stimulation (Fig. S4), thus indicating the possibility to modulate the neuronal firing rate. Importantly, control cells did not show any spiking activity associated with this level of mechanical stimulation (n= 15 cells), as would be expected given their lack of mechanical response. Thus, we were also able to exclude a direct cell-intrinsic dependence between the applied negative pressure and the increase in neuronal firing rate.

These experimental results illustrate the successful development of an *in-vitro* model efficiently expressing a functional bacterial MscL ion channel in mammalian neuronal networks.

Functional characterization of mechano-sensitized neuronal networks.

Since a lower activation pressure of the channel could lead to its potential spontaneous gating during cell reshaping and migration, and considering that mechanical cues play an important roles in network maturation, we evaluated the effect of G22S mutant expression in network development and physiology (Fig. 4A). In order to obtain the high percentage of eMscL-expressing neurons within the culture which is necessary for a network-level study, we infected neuronal cultures with the previously developed adeno associated virus expressing the G22S eMscL channel fused to tdTomato fluorescent protein.

Firstly, we compared cell viability and the number of synaptic contacts in control cell cultures and in neuronal networks expressing the eMscL channel. Analyses were performed on distinct fields of view acquired on each culture (Fig. 4B and 4C). As illustrated in Figure 4B, cell viability was preserved in networks expressing eMscL, thus indicating that eMscL membrane expression does not induce cell death (57±3% and 63±2% for the control and G22S neuronal networks, respectively). As a further control, we analyzed the viability of only the neurons expressing the G22S eMscL channel by staining of cell nuclei with propidium iodide dye. We again obtained cell viability of about 59±2% (n= 9 fields of view), which is consistent with the previous results.

Next, we quantified the number of glutamatergic and GABAergic synapses by immunostaining for the specific markers VGLUT1 (vesicular glutamate transporter 1) and VGAT (vesicular GABA transporter), respectively. Both the VGAT/VGLUT1 ratio (0.81±0.02, n= 6 fields of view for the control networks and 0.83±0.03, n= 8 fields of view for the eMscL expressing networks), and the number of excitatory and inhibitory synaptic puncta per cell (Fig. 4C, left and right panel respectively) did not show any significant differences between the control and the eMscL expressing networks. Therefore, we can conclude that expression of the eMscL channel does not alter the establishment of neuronal connections.

After having verified efficient development of our neuronal networks *in-vitro*, we monitored the spontaneous calcium activity after 20 DIV (Fig. 4D) using Fluo4 calcium dye. In Figure 4E, we report a representative trace of the normalized fluorescence calcium signal of a single neuron, indicated as $\Delta F/F_0$. The grey line is the raw calcium trace, and the superimposed black line is the result of the denoising algorithm (see methods section: Calcium imaging and data analysis).

The red dots indicate the onset times of the automatically detected calcium events. After extracting

and detecting the events of all cells identified within the field of view, we constructed a raster plot of the spontaneous neuronal network activity with single-cell resolution (Fig. 4F). We quantified the mean firing rate (MFR) of neuronal networks expressing the G22S eMscL channel and compared it to the MFR of control neuronal networks (n= 12 and 10 cell cultures, respectively). No significant change was detected between the two types of network (Fig. 4G, left panel). As a further control test, we also compared the MFRs of single neurons expressing the virally encoded eMscL construct (n= 917 cells) and control cells (n= 1380 cells), taken from the same network, confirming that the single cell MFR was unchanged upon eMscL expression (Fig. 4G, right panel). These results show that eMscL expression does not alter neuronal development and integration into a functional network.

Discussion

The powerful opportunities afforded by cell-type or tissue-specific sensitization to externally controlled stimuli, are inspiring the development and assessment of novel stimulation methods, based on either nanotechnology (Rivnay et al., 2017) and/or genetic engineering of cellular sensing elements. Moreover, the development of novel approaches to modulate the activity of neurons and deep brain circuits is pivotal to obtain fundamental understanding of brain (dys)functions, as well as for the design of effective therapeutic strategies to treat neurological disorders. In this regard, the advent of optogenetics has paved the way to the development of versatile experimental approaches inducing the sensitization of neuronal cells through the genetic expression of membrane ion channels with a specific gating response either to thermal, chemical or mechanical stimuli, just to mention some recent examples. An alternative route to achieve stimulus sensitization of tissues and cells is offered by the emerging field of nanotechnology (Rivnay et al., 2017). Smart nanoparticles are designed and developed to obtain a local enhancement of the stimulating field (Carugo et al., 2017; Marino et al., 2017), or a local transduction of the penetrating signal leading to the modulation of the cellular activities (Marino et al., 2015).

In this context, the exploitation of mechanical signals to remotely affect and control cellular functions is attracting considerable attention in research community. In fact, a mechanical signal could be easily transmitted deep through dense tissues, thus playing a key role in the modulation of mechano-dependent cellular pathways (Koser et al., 2016).

Here we show the use of the bacterial MscL channel to induce the mechano-sensitization of mammalian neuronal cells. Taking into account that MscL directly responds only to membrane tension without requiring any functional interaction with other cellular elements (Cox et al., 2016; Heureaux et al., 2014), we hypothesized that the heterologous expression of such bacterial MS ion channel in primary mammalian cells should not interfere with any intrinsic mechanotransduction

pathway of the cell. Therefore, we exploited the opportunity of potentially designing a new mechanotransduction pathway in mammalian cells.

It is worth noting that thanks to its detailed and broad biophysical characterization (Iscla and Blount, 2012), the MscL channel could be easily engineered (Liu, 2016). Indeed, well established procedures to change the mechanosensitivity, the channel conductance, and the gating mechanism of the MscL channel, are already available. For example, the substitution of the glycine residue at site 22, with more hydrophilic/hydrophobic residues, has been shown to decrease/increase the pressure threshold of the channel opening (Yoshimura et al., 1999).

The possibility to control and modify the sensitivity of the channel to mechanical signals is a key feature for the successful development of a mechanogenetic approach. Indeed, considering the analogy with optogenetics, where very few specialized cells present intrinsic sensitivity to light, it is nowadays established that all cells have some intrinsic mechanism of mechano-sensation, and that the brain itself behaves as a highly mechanosensitive organ (Tyler, 2012). Therefore, the fine tuning of the mechanosensitivity of the channel with respect to other cellular sensing elements and to the intensity of the mechanical signal, may represent an effective route to achieve specific activation of selected cellular targets, and thus overcome the limit of the intrinsic mechanosensitivity of cells. In this regard, two recent studies exploiting the pressure field generated by propagating US waves showed the possibility to achieve spatially resolved neuronal stimulation either by the genetic expression of MS channels (Ibsen et al., 2015), or the accurate design of the US propagating wavefront (Zhou et al., 2017). Therefore, the development of a cell-type specific stimulation approach would require both the expression of a MS channels with a well-tuned sensitivity, and the accurate shaping and calibration of the locally generated US pressure field. For the above reasons, we designed a viral vector encoding for the G22S MscL mutant, as its lower activation threshold may represent a required feature to achieve its selective activation through the use of low-intensity mechanical stimuli, which do not stimulate other cellular sensing elements.

Another distinctive property of the MscL channel is its nominal conductance (3 nS, (Kung et al., 2010)), which could be too high for neuronal cells. Nevertheless, the large conductance of the channel could represent a beneficial feature to accomplish shorter and gentler stimulation of cellular activity and, it could be modified accordingly through site-directed mutagenesis assay (Yang et al., 2012). Another characteristic of the MscL which is critical for its successful usage *in-vivo*, is that it is not ion selective and is not straightforward to change the selectivity of such a large pore. Indeed, the channel opening could produce a calcium influx which would elicit cellular apoptotic pathways. However, the use of MscL channel in mammalian cell cultures as a tool for the controlled delivery of bioactive molecules (Doerner et al., 2012) has been previously reported. The authors of this study

show that cell viability is preserved also for long temporal opening of the channel (in the order of few minutes) in presence of Ca^{2+} ions in the bath solution.

Nevertheless, our results and observations confirm that the heterologous expression of a functional bacterial MscL channel in primary neuronal cultures does not affect the cell survival, the neuronal network architecture, and the spontaneous network activity. Moreover, the generation of action potentials associated with the channel opening, upon application of a calibrated suction pressure, indicates successful mechano-sensitization of the neuronal cells, which could be used to induce and modulate neuronal activity upon mechanical stimulation. In this regard, it is important to highlight that the generation of action potential was only associated with the partial current response elicited upon the mechanical stimulation.

The required suction pressure to induce a partial response was about 145 mmHg, which correspond to about 0.02 MPa. Considering that the range of acoustic pressures which have previously demonstrated ability to elicit the activity of wild-type neuronal circuits is on the order of about 0.01÷0.1 MPa (Tufail et al., 2010; Tyler et al., 2008), i.e. well below the typical acoustic pressures inducing thermal or cavitation effects (Dalecki, 2004; Kubanek et al., 2016), we could deduce that the activation threshold of the eMscL channel is appropriate to accomplish its gating through the use of low-intensity US waves. However, the main challenge in achieving gating of a MS channel by US pressure wave, originates from a limited understanding of the underlying mechanisms of action, particularly concerning the interaction between low-intensity US waves and the biological matter (Plaksin et al., 2016), and the corresponding US field required to induce effective membrane strain. This has limited the identification of an optimal delivery of the US wavefront.

Finally, taking into account the advantages and drawbacks of stimulation approaches, it is worth noting how distinct combinations of core technologies, such as genetic engineering, nanotechnology (Rivnay et al., 2017), and DNA origami, to design ion channels is becoming a common practice to overcome current limitations. As an example, nanopore technologies could be employed to design novel membrane channels *de novo,* utilising a variety of building block materials (e.g. proteins, peptides, DNAs, synthetics and organics) in order to tailor specific pore structures and functions. However, building novel nanopore architectures is complex, and their assembly and interaction with the cell milieu is not fully predictable (Howorka, 2017). Therefore, the use of biological templates may represent a robust approach for engineering of the pore itself. The coding sequence of our modified bacterial MscL channel (eMscL) is optimized for mammalian neuronal expression and trafficking to the plasma membrane through the use of neuron-specific promoter and a voltage-gated channel targeting motif. For all the above reasons, we believe that the mammalian-engineered eMscL construct represents an important step forward for future applications in complex animal models, in

order to gain new insights into the mechanobiology of the nervous system (Koser et al., 2016), and to pave the way to the use of the eMscL ion channel as a mature tool for novel neuro-engineering applications.

Materials and Methods

Ethical approval

All procedures involving experimental animals were approved by the institutional IIT Ethic Committee and by the Italian Ministry of Health and Animal Care (Authorization number 110/2014-PR, December 19, 2014). When performing the experiments, we minimized the number of sacrificed animals and the potential for nociceptor activation and pain-like sensation, and respected the three Rs (replacement, reduction and refinement) principles, in accordance with the guidelines established by the European Community Council (Directive 2010/63/EU of 22 September 2010).

Primary neuronal cultures and transfection

Primary neurons were isolated from cortex tissues of Sprague Dawley rats at the embryonic age of 18 days. The female pregnant rats and mice were sacrificed through CO_2 suffocation and cervical dislocation, before the embryos extraction. Dissected tissues were dissociated by enzymatic digestion, incubating them in 0.25% Trypsin (Gibco) and 0.25 mg/ml bovine deoxyribonuclease I (Sigma-Aldrich) for 7 min at 37 °C. Before triturating the tissues with a P1000 pipette tip, an equal volume of Dulbecco's Modified Eagle Medium (DMEM, Gibco) supplemented with 10% Fetal Bovine Serum (FBS, Gibco) was added to the suspension for blocking the trypsin activity. Isolated cortical neurons were counted and plated at a final density of 300 cells/mm^2 or 500 cells/mm^2 onto 18 mm glass coverslips.

Before use, glass coverslips were cleaned and overnight pre-coated with 0.1% Poly-D-lysine (PDL, Sigma) in order to enhance cell adhesion.

Neurons were grown in neuronal medium containing Neurobasal medium (NB, Gibco) supplemented with 2% B27 supplement (Gibco) and 1% GlutaMAX (Gibco) at 37°C/5% CO_2 humidified atmosphere. Cultures were maintained up to 25 days in vitro (DIV) and fresh medium was added weekly (about 300µL) to avoid changing in osmolarity due to the medium evaporation.

Primary neuronal cells were transfected at 2 DIV with 0.4 µg of MscL plasmid and/or 0.7 µg of myristoylated GFP plasmid (myr-GFP) with Lipofectamine 2000 transfection reagent (Invitrogen). A DNA to Lipofectamine ratio of 1 to 1 in a final volume of 300 µl was used for each well. Cells

were incubated for 40 minutes at 37°C/5% CO2 with DNA lipofectamine complexes, after which the culture media was completely removed and replaced with a pre-warmed neuronal medium.

MscL-v.1 and MscL-v.2 constructs

pAAV-hSyn1-MscL-eGFP-v.1 construct. The MscL cDNAs, kindly provided by Dr. Boris Martinac (Victor Chang Cardiac Research Institute, Darlinghurst, Australia), was excised from pTRE-Tight (Clontech) source plasmid and sub-cloned in-frame with eGFP into pAAV-hSyn1-eGFP vector through the SalI and BamHI restriction sites.

Engineering pAAV-hSyn1-MscL-tdTomato-v.2. In order to get a more specific membrane targeting of MscL channel, a second generation of the construct was built by adding at C-terminus of our construct the sequence encoding the Kir2.1 endoplasmic reticulum export signal (ERexp) as previously described (Gradinaru et al., 2010). Then, the eGFP protein was replaced with a tdTomato protein, known for having a brighter fluorescence signal. From section: "Electrophysiological characterization of the mammalian-engineered MscL channel functionality", we refer to the pAAV-hSyn1-MscL-tdTomato-v.2 as enhanced-MscL (eMscL).

Patch-clamp recordings and pressure-clamp system

Primary cortical neurons were plated at a density of 300 cells/mm^2 onto 18 mm glass coverslip and the voltage-clamp recording was performed in cell-attached configuration between 14 and 20 DIV.
Borosilicate glass capillary (1.50 mm OD/0.86 mm ID, KF Technology) were pulled using an horizontal puller (P1000, Sutter Instruments) with a resistance in the range of 6 and 10 MOhms, to generate a glass pipette.
The cell-attached experiments were performed applying a command potential of +30 mV and, assuming a resting potential of -70 mV, the estimated applied potential would be -100 mV. Current traces were inverted according to common convention for cell-attached recordings. The bath solution contained 140 mM NaCl, 3 mM KCl, 1 mM $MgCl_2$, 1 mM $CaCl_2$ and 10 mM HEPES (pH 7.2); the pipette solution contained 140 mM NaCl, 0.5 mM $CaCl_2$, 2 mM EGTA and 10 mM HEPES (pH 7.2). EGTA was added for buffering free Ca^{2+}. The eMscL-induced currents were amplified through the MultiClamp 700B amplifier (Axon Instruments), and then digitized and recorded with the Digidata 1200A (Axon Instruments) acquisition board. The output current signals were sampled at 25 kHz and filtered using a low-pass filter frequency of 10 kHz.
In order to apply a calibrated negative pressure during the voltage-clamp recording, the setup was equipped with a custom-made pressure sensor system. It comprised a silicon piezo resistive pressure

sensor (model MPDX2200DP, Freescale), which generated a linear voltage output directly proportional to the pressure applied in the tubing connected to the patch pipette. The pressure sensor system was connected to a custom-made conditioning circuit and acquired through the MultiClamp 700B amplifier (Molecular Devices). The active conditioning circuit performed amplification, balancing, level shifting and offset compensation of the differential output (temperature and drift compensation) of the pressure sensor, and it was based on a double stage operational amplifier circuitry with onboard offset and gain controls. The output voltage to pressure conversion factor of the overall pressure sensor system was calibrated with a pipette perfusion instrument (2PK+, ALA Scientific Instruments), which was used to apply well-defined negative pressures (in mmHg) to the tubing connected to the patch pipette. During the experiments, the pressure in the tubing was manually applied through a 5 mL luer-lock syringe, and monitored in real time through the pCLAMP 10 software (Molecular Devices).

Data acquisition and analysis were controlled using the pCLAMP 10 software package. The pressure activation threshold was determined by observing at which pressure the first evoked-current or a relevant change in the trace slope occurred. Data were filtered with low-pass Bessel filter before the analysis. To verify that the recorded spikes were indeed action potentials, we added 1 μM TTX (Tocris Bioscience) to the bath solution and incubated for 5 minutes to block Na^+ channels, before applying the negative pressure through the patch pipette.

Estimating the applied membrane tension

Since the lack of a highly resolved image of the membrane dome into the pipette patch, we estimated the tension elicited along the plasma membrane upon the mechanical stimulation by applying an equation based on the Laplace's law previously reported in literature (Ursell et al., 2011).

The membrane tension (τ) was estimated using the equation $\tau = \gamma + (r \cdot P)/2$, where r is the radius of pipette tip (approximately 1 μm) and P is the applied negative pressures in terms of $mN \cdot m^{-2}$.

Immunostaining and image analysis

For co-localization and morphological analyses, neuronal cells were fixed at 15 DIV, and for immunostaining with synaptic markers, cells were fixed at 18-20 DIV.

Neurons were fixed in 4% cold paraformaldehyde (PFA, Sigma-Aldrich) in standard phosphate-buffered saline (PBS, Sigma-Aldrich) for 15 minutes at RT, washed twice in 1X TBS and mounted with ProLong Diamond Antifade mountant (Invitrogen).

For immunostaining, after the fixation protocols was completed cells were permeabilized with 0.1% Triton X-100 (Sigma-Aldrich) in 1X tris-buffered saline (TBS) for 5 minutes at RT, and then blocked with 3% bovine serum albumin (BSA, Sigma-Aldrich) in 1X TBS for 1 hour at RT.

Immunostaining was performed by incubating the primary antibody overnight at 4°C and, after few washing steps in 1X TBS, incubating the secondary antibody for 1 hour at RT. During the labelling with secondary antibodies, cells were covered with a silver foil to preserve the sample from light. Primary antibodies were: guinea pig anti-VGLUT1 (135304, SYSY), rabbit anti-VGAT (131013, SYSY), and neuronal class III beta-tubulin antibody (MMS-435P, Covance) diluted respectively 1:500, 1:1000 and 1:250. Secondary antibodies were: Alexa Fluor 488 goat anti-guinea pig IgG (A11073, Life Technologies), and Alexa Fluor 568 goat anti-rabbit IgG (A11036, Life Technologies). All secondary antibodies were diluted 1:1000. Primary and secondary antibodies were diluted in 3% BSA in 1X TBS.

Images were acquired on a Leica SP8 confocal microscope (Leica Microsystems) and analyzed with ImageJ, except where otherwise specified.

For neuronal morphology analysis, images were acquired on the DeltaVision Elite microscope (GE Healthcare Life Sciences) using a 20X air objective (PLN 20X/0.4, Olympus). The analysis was performed by running the morphology quantification software NeurphologyJ, an ImageJ plugin, as described in Ho et al., 2011 (Ho et al., 2011).

Co-localization analysis was performed by using the Coloc2 Image plugin, by following the described procedure (Costes et al., 2004).

Viability plot was calculated as mean of the percentage of live cells divided by the total number of cells for field of view, as described in Palazzolo et al., 2017 (Palazzolo et al., 2017). The apoptotic cells, which are characterized by pyknotic nuclei, were identified by their morphology and counted.

Adeno associated virus production

AAV-eMscL particles production was performed in 15-cm culture dishes by using a total amount of $25x10^6$ HEK293T cells ($5x10^6$ per dish). The transfections were carried out at 70% confluence by using a standard calcium phosphate-based protocol. The transfected DNAs consisted of a 1:1:1 ratio mixture of AAV vector plasmid, AAV serotype 1 and 2 packaging proteins (pRV1 and pH21), and adenoviral helper (pFdelta6). Seventy-two hours after transfection cells were harvested and AAV particles were extracted by subjecting the cell pellet to three consecutive freeze-thaw cycles and purified through a heparin column (Hitrap Heparin, GE Healthcare).

Calcium imaging and data analysis

The primary neuronal cultures were infected with a recombinant adeno associated virus (hybrid serotype 1 and 2) encoding the G22S eMscL ion channel. Primary cultures were infected at 15 DIV by incubating overnight 1:1000 dilution of the virus stock solution. After incubation, the culture medium was half replaced with a fresh one.

The infected cell cultures showed a good level of protein expression together with a significant calcium activity starting from 5 days post infection. Calcium imaging experiments were assayed between 20 and 25 DIV, after loading the cell cultures with Fluo-4 AM calcium dye (Invitrogen) for 20 minutes.

Calcium imaging was performed by using a custom inverted fluorescence microscope which has been integrated with a miniaturized cell incubator (Aviv et al., 2013). The time-lapse calcium imaging was performed at a frame rate of 65 Hz through a 10x air objective (NA 0.25, Olympus), 2x2 binning, and EM gain of 120. The acquired time lapse imaging series (t-stack series) were analyzed with a custom written algorithm in MATLAB, which have been previously described (Palazzolo et al., 2017).

Briefly, the algorithm computed the standard deviation projection of the t-stack and the non-homogeneous background in the projection image was estimated through a morphological opening operation with a disk of arbitrary size (smaller than the typical dimension of the cell soma), and then subtracted. Successively, the projection image was binarized, and the ROIs were detected. The fluorescence calcium traces of the neurons were then extracted from the t-stack by computing the mean fluorescence intensity value within the ROIs previously identified. Subsequently, the raw traces of the neurons were baseline corrected and normalized, to calculate the normalized fluorescent calcium signals indicated as $\Delta F/F_0$ (F fluorescence intensity in a.u.). The baseline F_0 of the traces was automatically estimated with a linear diffusion filter, which evaluates only the slow varying component of the trace by setting a large time window (time window length=30 s). The normalized traces were then smoothed with the modified Perona-Malik filter (Palazzolo et al., 2017).

On the smoothed traces, calcium events were automatically detected by imposing the following conditions: (i) the first derivative in a right interval of the onset overcomes a fixed positive threshold (10^{-3} in case of asynchronous activity, 10^{-2} in case of synchronous activity); (ii) the ΔF between the onset and the offset of an event overcomes a threshold defined as the standard deviation of the difference between the original and the smoothed trace; (iii) the first derivative in a right interval of the event offset is lower than a fixed negative threshold (-10^{-4}); and (iv) the time interval between the last time point after the onset with first derivative higher than a fixed threshold and the offset did not reach a fixed width (300 time points).

Data analysis

Statistical analysis, graphs and plots were generated using GraphPad Prism 6 (GraphPad Software) and MATLAB 2016b (MathWorks). To verify if our data sets were reflecting a normal distribution, the Shapiro-Wilk normality test was carried out. Since the normality distribution was not fulfilled, the statistical significance analysis was performed using the nonparametric two-sided Mann-Whitney test ($p= 0.05$) and data set given as mean ± SEM.

Acknowledgements

We thank Boris Martinac (Victor Chang Cardiac Research Institute, Darlinghurst, Australia) for kindly providing the *E. coli* WT and G22S MscL constructs. We thank Massimo Vassalli for evaluable discussions and suggestions. We thank Marina Nanni for the technical assistance in cell culture preparation, Alessandro Parodi and Giacomo Pruzzo for the development of electronic and software interfaces to perform pressure/voltage clamp recording and calcium imaging. We also thank Annalisa Savardi, Caterina Gasperini, Marco Nigro, Ali Mosayyebi and Prutha Patel, who provided scientific support and critical commentaries during the study. Finally, we thank Tommaso Fellin for critical reading of the manuscript.

G.I.H. was supported by Alzheimer's Research UK, K.D. was supported by the BBSRC (BB/L007576/1). G.P. was supported by Compagnia di San Paolo (grant agreement n. EPFD0041). A.S. and M.M. by IIT intramural funds.

Author contributions

A.S. performed all the experiments; A.S. and A.B. designed and performed the data analysis of electrophysiological recordings; A.S. and A.C. designed and performed the molecular engineering of the eMscL construct; A.S., M.M., G.P. and F.D. performed calcium imaging experiments and data analysis; G.I.H., J.C., K.D. and D.C. supervised the morphological analysis of neuronal networks, and provided a critical revision of the project; A.S., A.B. and F.D. wrote the manuscript; all the authors revised the manuscript; F.D. conceived the project and supervised the study.

Conflict of interest

The authors declare no conflict of interest.

References

Armbruster, B. N., Li, X., Pausch, M. H., Herlitze, S. and Roth, B. L. (2007). Evolving the lock to fit the key to create a family of G protein-coupled receptors potently activated by an inert ligand. *Proc. Natl. Acad. Sci.* **104**, 5163–5168.

Aviv, M. S., Pesce, M., Tilve, S., Chieregatti, E., Zalevsky, Z. and Difato, F. (2013). Motility flow and growth-cone navigation analysis during in vitro neuronal development by long-term bright-field imaging. *J. Biomed. Opt.* **18**, 111415.

Beltramo, R., D'Urso, G., Maschio, M. D., Farisello, P., Bovetti, S., Clovis, Y., Lassi, G., Tucci, V., De Pietri Tonelli, D. and Fellin, T. (2013). Layer-specific excitatory circuits differentially control recurrent network dynamics in the neocortex. *Nat. Med.* **16**, 1–10.

Carugo, D., Aron, M., Sezgin, E., Bernardino de la Serna, J., Kuimova, M. K., Eggeling, C. and Stride, E. (2017). Modulation of the molecular arrangement in artificial and biological membranes by phospholipid-shelled microbubbles. *Biomaterials* **113**, 105–117.

Cash, S. S. and Hochberg, L. R. (2015). The Emergence of Single Neurons in Clinical Neurology. *Neuron* **86**, 79–91.

Coste, B., Xiao, B., Santos, J. S., Syeda, R., Grandl, J., Spencer, K. S., Kim, S. E., Schmidt, M., Mathur, J., Dubin, A. E., et al. (2012). Piezo proteins are pore-forming subunits of mechanically activated channels. *Nature* **483**, 176–181.

Costes, S. V, Daelemans, D., Cho, E. H., Dobbin, Z., Pavlakis, G. and Lockett, S. (2004). Automatic and quantitative measurement of protein-protein colocalization in live cells. *Biophys. J.* **86**, 3993–4003.

Cox, C. D., Bae, C., Ziegler, L., Hartley, S., Nikolova-Krstevski, V., Rohde, P. R., Ng, C.-A., Sachs, F., Gottlieb, P. A. and Martinac, B. (2016). Removal of the mechanoprotective influence of the cytoskeleton reveals PIEZO1 is gated by bilayer tension. *Nat. Commun.* **7**, 10366.

Dalecki, D. (2004). Mechanical Bioeffects of Ultrasound. *Annu. Rev. Biomed. Eng.* **6**, 229–248.

Doerner, J. F., Febvay, S. and Clapham, D. E. (2012). Controlled delivery of bioactive molecules into live cells using the bacterial mechanosensitive channel MscL. *Nat. Commun.* **3**, 990.

Fregni, F. and Pascual-Leone, A. (2007). Technology insight: noninvasive brain stimulation in neurology-perspectives on the therapeutic potential of rTMS and tDCS. *Nat. Clin. Pract. Neurol.* **3**, 383–393.

Gradinaru, V., Thompson, K. R. and Deisseroth, K. (2008). eNpHR: A Natronomonas halorhodopsin enhanced for optogenetic applications. *Brain Cell Biol.* **36**, 129–139.

Gradinaru, V., Zhang, F., Ramakrishnan, C., Mattis, J., Prakash, R., Diester, I., Goshen, I., Thompson, K. R. and Deisseroth, K. (2010). Molecular and Cellular Approaches for Diversifying and Extending Optogenetics. *Cell* **141**, 154–165.

Grill, W. M., Norman, S. E. and Bellamkonda, R. V. (2009). Implanted Neural Interfaces: Biochallenges and Engineered Solutions. *Annu. Rev. Biomed. Eng.* **11**, 1–24.

Grossman, N., Bono, D., Dedic, N., Kodandaramaiah, S. B., Rudenko, A., Suk, H. J., Cassara, A. M., Neufeld, E., Kuster, N., Tsai, L. H., et al. (2017). Noninvasive Deep Brain Stimulation via Temporally Interfering Electric Fields. *Cell* **169**, 1029–1041.e16.

Hamill, O. P. and Martinac, B. (2001). Molecular Basis of Mechanotransduction in Living Cells. *Physiol. Rev.* **81**, 685–740.

Hertzberg, Y., Naor, O., Volovick, A. and Shoham, S. (2010). Towards multifocal ultrasonic neural stimulation: pattern generation algorithms. *J. Neural Eng.* **7**, 56002.

Heureaux, J., Chen, D., Murray, V. L., Deng, C. X. and Liu, A. P. (2014). Activation of a Bacterial Mechanosensitive Channel in Mammalian Cells by Cytoskeletal Stress. *Cell. Mol. Bioeng.* **7**, 307–319.

Ho, S.-Y., Chao, C.-Y., Huang, H.-L., Chiu, T.-W., Charoenkwan, P. and Hwang, E. (2011). NeurphologyJ: an automatic neuronal morphology quantification method and its application in pharmacological discovery. *BMC Bioinformatics* **12**, 230.

Hofherr, A. (2005). Selective Golgi export of Kir2.1 controls the stoichiometry of functional Kir2.x channel heteromers. *J. Cell Sci.* **118**, 1935–1943.

Howorka, S. (2017). Building membrane nanopores. *Nat. Nanotechnol.* **12**, 619–630.

Ibsen, S., Tong, A., Schutt, C., Esener, S. and Chalasani, S. H. (2015). Sonogenetics is a non-invasive approach to activating neurons in Caenorhabditis elegans. *Nat. Commun.* **6**, 8264.

Iscla, I. and Blount, P. (2012). Sensing and Responding to Membrane Tension: The Bacterial

MscL Channel as a Model System. *Biophys. J.* **103**, 169–174.

Iscla, I., Eaton, C., Parker, J., Wray, R., Kovács, Z. and Blount, P. (2013). Improving the design of a MscL-based triggered nanovalve. *Biosensors* **3**, 171–184.

Jorfi, M., Skousen, J. L., Weder, C. and Capadona, J. R. (2015). Progress towards biocompatible intracortical microelectrodes for neural interfacing applications. *J. Neural Eng.* **12**, 11001.

Kloda, A., Petrov, E., Meyer, G. R., Nguyen, T., Hurst, A. C., Hool, L. and Martinac, B. (2008). Mechanosensitive channel of large conductance. *Int. J. Biochem. Cell Biol.* **40**, 164–9.

Kocer, A. (2005). A Light-Actuated Nanovalve Derived from a Channel Protein. *Science (80-.).* **309**, 755–758.

Koser, D. E., Thompson, A. J., Foster, S. K., Dwivedy, A., Pillai, E. K., Sheridan, G. K., Svoboda, H., Viana, M., Costa, L. da F., Guck, J., et al. (2016). Mechanosensing is critical for axon growth in the developing brain. *Nat. Neurosci.* **19**, 1592–1598.

Krasovitski, B., Frenkel, V., Shoham, S. and Kimmel, E. (2011). Intramembrane cavitation as a unifying mechanism for ultrasound-induced bioeffects. *Proc. Natl. Acad. Sci. U. S. A.* **108**, 3258–63.

Krishna, V., Sammartino, F. and Rezai, A. (2017). A Review of the Current Therapies, Challenges, and Future Directions of Transcranial Focused Ultrasound Technology. *JAMA Neurol.*

Kubanek, J., Shi, J., Marsh, J., Chen, D., Deng, C. and Cui, J. (2016). Ultrasound modulates ion channel currents. *Sci. Rep.* **6**, 24170.

Kung, C., Martinac, B. and Sukharev, S. (2010). Mechanosensitive Channels in Microbes. *Annu. Rev. Microbiol.* **64**, 313–329.

Li, D., Takimoto, K. and Levitan, E. S. (2000). Surface expression of Kv1 channels is governed by a C-terminal motif. *J. Biol. Chem.* **275**, 11597–11602.

Li, T., Chen, Y. and Ma, J. (2009). Development of a miniaturized piezoelectric ultrasonic transducer. *IEEE Trans. Ultrason. Ferroelectr. Freq. Control* **56**, 649–659.

Liu, A. P. (2016). Biophysical Tools for Cellular and Subcellular Mechanical Actuation of Cell Signaling. *Biophys. J.* **111**, 1112–1118.

Marino, A., Arai, S., Hou, Y., Sinibaldi, E., Pellegrino, M., Chang, Y., Mazzolai, B., Mattoli, V., Suzuki, M. and Ciofani, G. (2015). Piezoelectric Nanoparticle-Assisted Wireless Neuronal Stimulation. *ACS Nano* **9**, 7678–7689.

Marino, A., Arai, S., Hou, Y., Degl'Innocenti, A., Cappello, V., Mazzolai, B., Chang, Y. T., Mattoli, V., Suzuki, M. and Ciofani, G. (2017). Gold Nanoshell-Mediated Remote Myotube Activation. *ACS Nano* **11**, 2494–2505.

Martinac, B. (2014). The ion channels to cytoskeleton connection as potential mechanism of mechanosensitivity. *Biochim. Biophys. Acta - Biomembr.* **1838**, 682–691.

Martinac, B., Nomura, T., Chi, G., Petrov, E., Rohde, P. R., Battle, A. R., Foo, A., Constantine, M., Rothnagel, R., Carne, S., et al. (2014). Bacterial mechanosensitive channels: models for studying mechanosensory transduction. *Antioxid. Redox Signal.* **20**, 952–69.

Maurer, J. A. and Dougherty, D. A. (2003). Generation and evaluation of a large mutational library from the Escherichia coli mechanosensitive channel of large conductance, MscL. Implications for channel gating and evolutionary design. *J. Biol. Chem.* **278**, 21076–21082.

Meister, M. (2016). Physical limits to magnetogenetics. *Elife* **5**,.

Palazzolo, G., Moroni, M., Soloperto, A., Aletti, G., Naldi, G., Vassalli, M., Nieus, T. and Difato, F. (2017). Fast wide-volume functional imaging of engineered in vitro brain tissues. *Sci. Rep.* **7**, 8499.

Panzeri, S., Harvey, C. D., Piasini, E., Latham, P. E. and Fellin, T. (2017). Cracking the Neural Code for Sensory Perception by Combining Statistics, Intervention, and Behavior. *Neuron* **93**, 491–507.

Plaksin, M., Kimmel, E. and Shoham, S. (2016). Cell-Type-Selective Effects of Intramembrane Cavitation as a Unifying Theoretical Framework for Ultrasonic Neuromodulation. *eNeuro* **3**, 1–16.

Rivnay, J., Wang, H., Fenno, L., Deisseroth, K. and Malliaras, G. G. (2017). Next-generation probes, particles, and proteins for neural interfacing. *Sci. Adv.* **3**, e1601649.

Rogan, S. and Roth, B. (2011). Remote control of neuronal signaling. *Pharmacol. Rev.* **63**, 291–315.

Rosholm, K. R., Baker, M. A. B., Ridone, P., Nakayama, Y., Rohde, P. R., Cuello, L. G., Lee, L. K. and Martinac, B. (2017). Activation of the mechanosensitive ion channel MscL by mechanical stimulation of supported Droplet-Hydrogel bilayers. *Sci. Rep.* **7**, 1–10.

Sawada, Y., Murase, M. and Sokabe, M. (2012). The gating mechanism of the bacterial mechanosensitive channel MscL revealed by molecular dynamics simulations: from tension sensing to channel opening. *Channels (Austin).* **6**, 317–331.

Soloperto, A., Bisio, M., Palazzolo, G., Chiappalone, M., Bonifazi, P. and Difato, F. (2016). Modulation of Neural Network Activity through Single Cell Ablation: An in Vitro Model of Minimally Invasive Neurosurgery. *Molecules* **21**, 1018.

Stockklausner, C., Ludwig, J., Ruppersberg, J. . and Klöcker, N. (2001). A sequence motif responsible for ER export and surface expression of Kir2.0 inward rectifier K + channels. *FEBS Lett.* **493**, 129–133.

Suchyna, T. M., Markin, V. S. and Sachs, F. (2009). Biophysics and structure of the patch and the gigaseal. *Biophys. J.* **97**, 738–747.

Sukharev, S. I., Blount, P., Martinac, B., Blattner, F. R. and Kung, C. (1994). A large-conductance mechanosensitive channel in E. coli encoded by mscL alone. *Nature* **368**, 265–268.

Sukharev, S. I., Blount, P., Martinac, B. and Kung, C. (1997). MECHANOSENSITIVE CHANNELS OF ESCHERICHIA COLI : The MscL Gene , Protein , and Activities.

Tay, A. and Di Carlo, D. (2017). Magnetic Nanoparticle-Based Mechanical Stimulation for Restoration of Mechano-Sensitive Ion Channel Equilibrium in Neural Networks. *Nano Lett.* **17**, 886–892.

Tay, A., Kunze, A., Murray, C. and Di Carlo, D. (2016). Induction of Calcium Influx in Cortical Neural Networks by Nanomagnetic Forces. *ACS Nano* **10**, 2331–2341.

Tufail, Y., Matyushov, A., Baldwin, N., Tauchmann, M. L., Georges, J., Yoshihiro, A., Tillery, S. I. H. and Tyler, W. J. (2010). Transcranial Pulsed Ultrasound Stimulates Intact Brain Circuits. *Neuron* **66**, 681–694.

Tyler, W. J. (2011). Noninvasive neuromodulation with ultrasound? A continuum mechanics hypothesis. *Neuroscientist* **17**, 25–36.

Tyler, W. J. (2012). The mechanobiology of brain function. *Nat. Rev. Neurosci.* **13**, 867–878.

Tyler, W. J., Tufail, Y., Finsterwald, M., Tauchmann, M. L., Olson, E. J. and Majestic, C. (2008). Remote Excitation of Neuronal Circuits Using Low-Intensity, Low-Frequency Ultrasound. *PLoS One* **3**, e3511.

Ursell, T., Agrawal, A. and Phillips, R. (2011). Lipid bilayer mechanics in a pipette with glass-bilayer adhesion. *Biophys. J.* **101**, 1913–1920.

Wang, Y. and Guo, L. (2016). Nanomaterial-enabled neural stimulation. *Front. Neurosci.* **10**, 1–7.

Wheeler, M. A., Smith, C. J., Ottolini, M., Barker, B. S., Purohit, A. M., Grippo, R. M., Gaykema, R. P., Spano, A. J., Beenhakker, M. P., Kucenas, S., et al. (2016). Genetically targeted magnetic control of the nervous system. *Nat. Neurosci.* **19**, 756–761.

Whissell, P. D., Tohyama, S. and Martin, L. J. (2016). The use of DREADDs to deconstruct behavior. *Front. Genet.* **7**, 1–15.

Yang, L.-M., Wray, R., Parker, J., Wilson, D., Duran, R. S. and Blount, P. (2012). Three Routes To Modulate the Pore Size of the MscL Channel/Nanovalve. *ACS Nano* **6**, 1134–1141.

Yoshimura, K., Batiza, A., Schroeder, M., Blount, P. and Kung, C. (1999). Hydrophilicity of a single residue within MscL correlates with increased channel mechanosensitivity. *Biophys. J.* **77**, 1960–72.

Zhou, W., Wang, J., Wang, K., Huang, B., Niu, L., Li, F., Cai, F., Chen, Y., Liu, X., Zhang, X., et al. (2017). Ultrasound neuro-modulation chip: activation of sensory neurons in Caenorhabditis elegans by surface acoustic waves. *Lab Chip* **17**, 1725–1731.

Figures

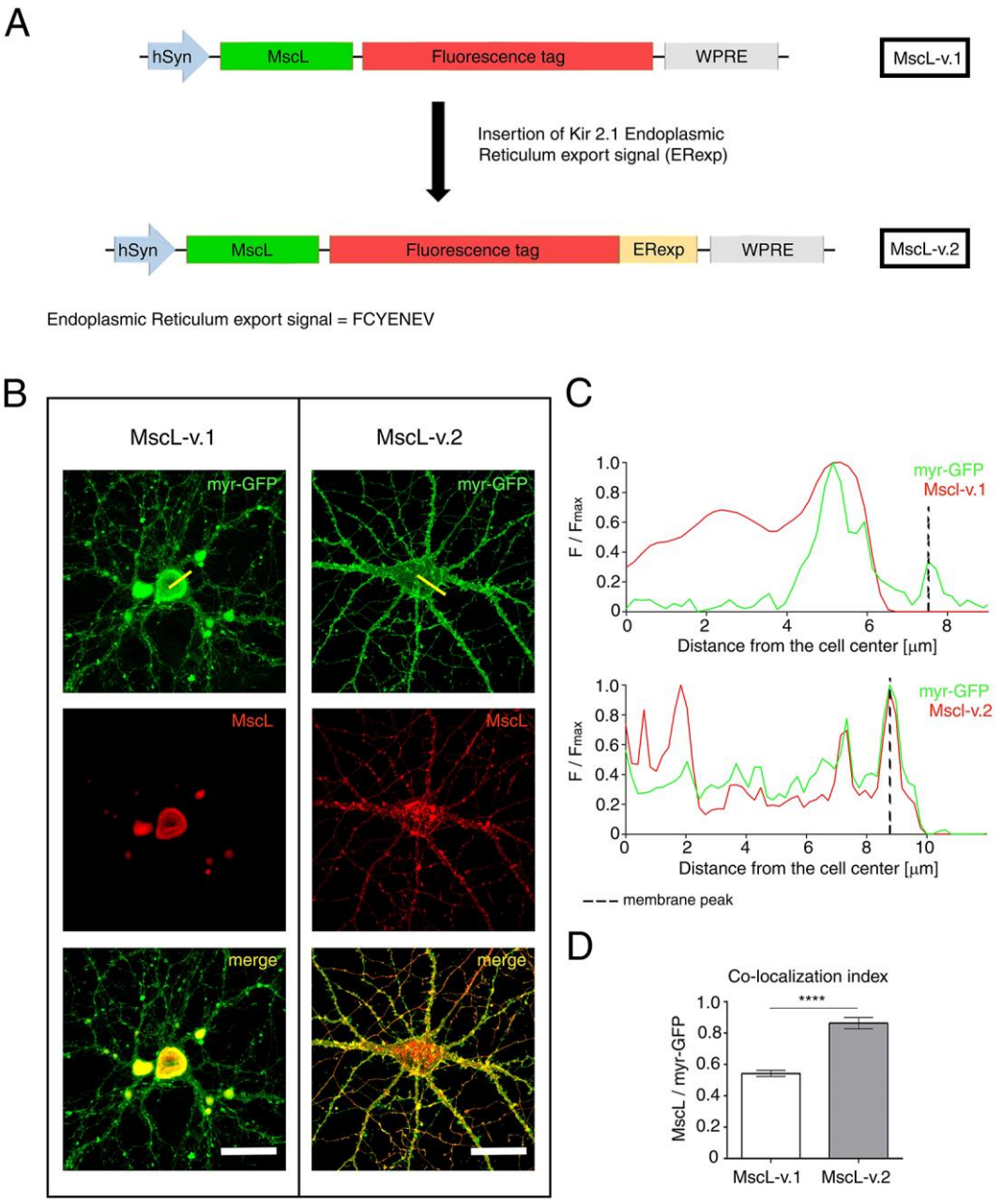

Fig. 1. Membrane targeting of the mammalian-engineered MscL-v.2 ion channel.

A. Construct map of the MscL-v.1 (top) and MscL-v.2 (bottom) plasmid in AAV vectors. MscL-v.2 is optimized for expression in mammalian primary neurons.

B. Cortical primary neurons expressing the MscL-v.1 (left) and MscL-v.2 (right) constructs. Myristoylated GFP (green) and MscL fused to tdTomato (red), and their fluorescence signal merged (yellow) are shown to illustrate the reduced aggregation of MscL in ER (endoplasmic reticulum), as

well as its improved membrane expression after addition of the Kir2.1 ER export signal. Scale bar: 50 μm.

C. Normalized fluorescence intensity profile of the myr-GFP with either the MscL-v.1 (top) or MscL-v.2 (bottom). The intensity profiles are extracted along the yellow cross-sectional line reported in panel B.

D. Co-localization analysis of the myr-GFP with either the MscL-v.1 or the MscL-v.2 channel. The signal of the myr-GFP is correlated more strongly with the MscL-v.2 ($r = 0.86 \pm 0.04$, $n = 8$) when compared to MscL-v.1 ($r = 0.54 \pm 0.02$, $n = 11$), at the membrane edge. Values are reported as mean ± standard errors of the mean (SEM). The difference between the means of the two data sets is statistically significant, with a p value < 0.0001.

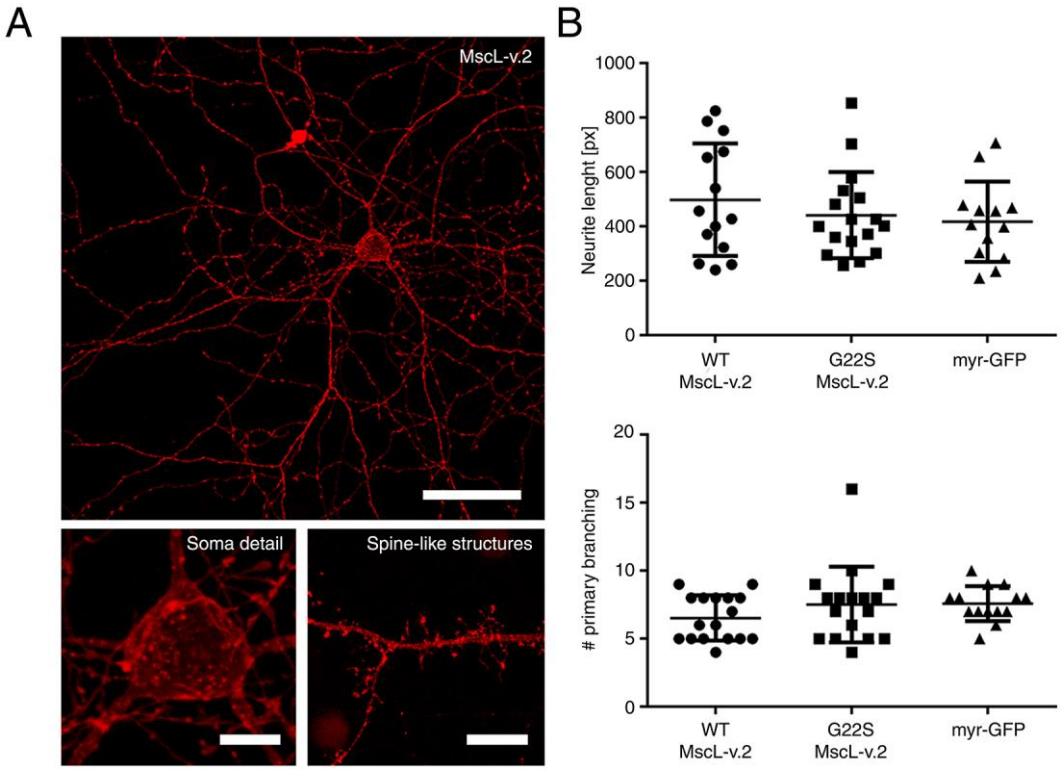

Fig. 2. Morphological evaluation of neuron expressing MscL-v.2 construct.

A. Maximum projection of a confocal z-stack of a primary cortical neuron expressing MscL-v.2 fused to tdTomato fluorescent protein (scale bar= 50 μm). The bottom images show the MscL-v.2 fluorescence signal in the soma (left, scale bar= 10 μm) and spine-like structures (bottom right, scale bar= 10 μm).

B. In the upper panel, quantification of the neurite length of neurons expressing the WT MscL-v.2 (490.30±55.20, n= 14) or the G22S MscL-v.2 (441.50±38.33, n=17) or the myr-GFP (417.10±41.00, n= 13). The data are presented in terms of number of pixels and no statistically significant difference was measured. In the lower panel, quantification of the number of primary neuronal branches calculated for each construct (WT MscL-v.2: 6.53±0.41, n= 17; G22S MscL-v.2: 7.53±0.68, n=17; myr-GFP: 7.57±0.34, n=14) is reported. Values are reported as mean ± SEM and no statistically significant difference was measured.

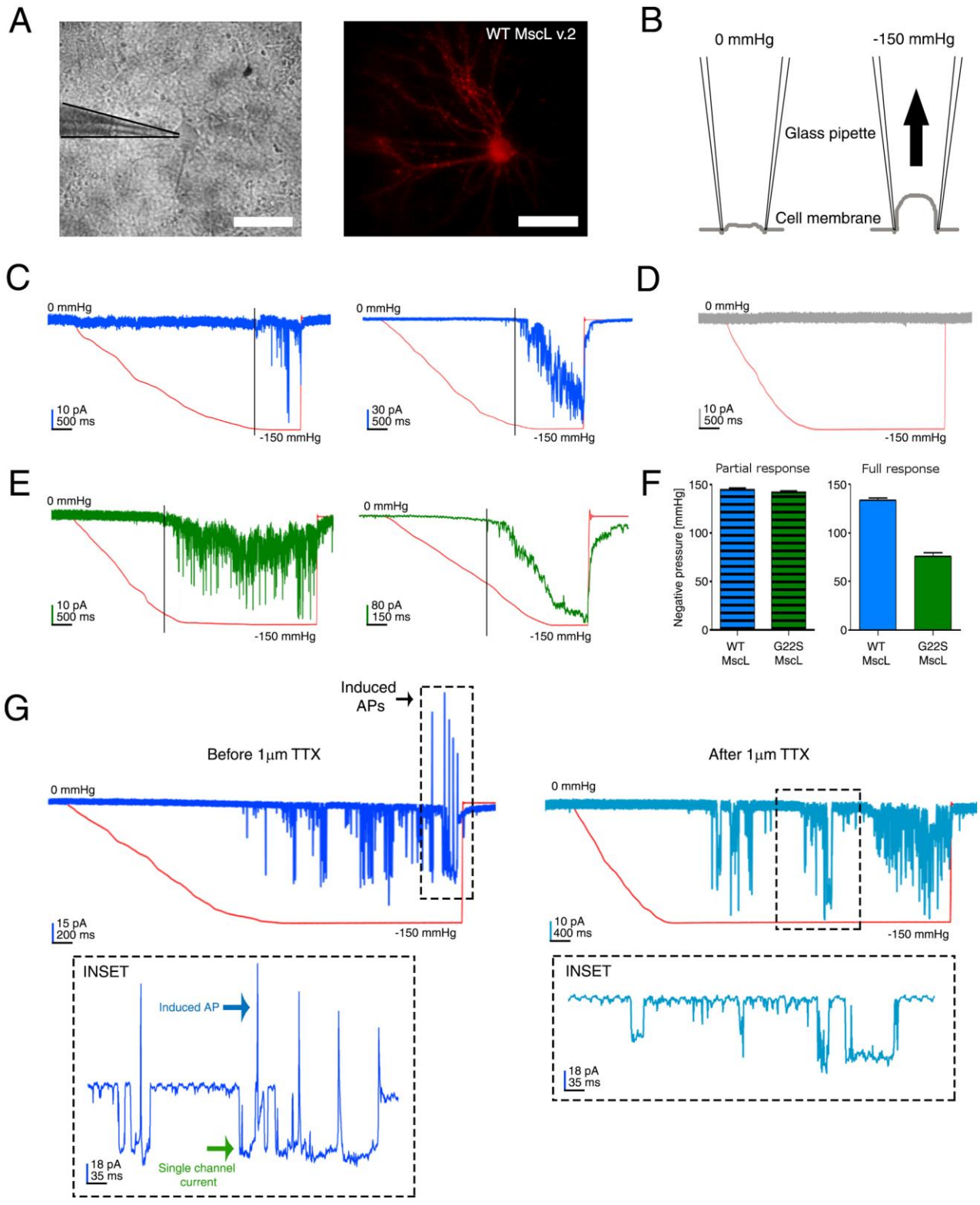

Fig. 3. Electrophysiological characterization of the eMscL channel expressed in primary cortical neurons.

A. Bright field (left) and fluorescence image (right) of a patched cortical neuron (15 DIV) expressing the eMscL construct. The red fluorescence signal is due to the tdTomato fluorescent protein encoded by the eMscL construct. Scale bars= 50 μm.

B. Cartoon indicating the procedure to perform pressure/voltage-clamp recording in cell-attached configuration during pressure-clamp stimulation. Application of a negative pressure induces the cell membrane stretch, which activates the gating of the eMscL channel. During the stimulation, a command potential of +30 mV was applied, and, assuming a resting potential of -70 mV, the estimated applied potential is -100 mV.

C. Traces of the recorded ion currents (blue trace) during pressure stimulation (red trace) of the membrane patch, in a neuron expressing the WT eMscL channel. On the left, the trace reports a typical example of recorded ionic currents during a partial response. On the right, the current trace of an example of recorded full response.

D. Example of recorded ion current (gray trace) during pressure/voltage-clamp recording of a control neuron expressing only the tdTomato fluorescent protein.

E. Recorded ion currents (green trace) during the pressure stimulation of a neuron expressing the G22S eMscL channel. On the left, the trace reports a typical example of recorded partial response. On the right, the trace is a representative recording of a full response.

F. Bar plots reporting the quantification of the pressure activation threshold required to trigger the WT and G22S eMscL-induced currents. On the left, the quantification of the pressure threshold gating the partial response (145±0.98 mmHg, N= 72 stimulation trials, on n= 19 cells, and 142.50±0.91 mmHg, N= 111 stimulation trials, on n= 24 cells, for the WT and G22S channel respectively). On the right, the quantification of the pressure threshold histogram gating the full response (130±2.36, N= 48, on n= 10 cells, and 75.78±3.60, N= 67 stimulation trials, on n= 17 cells, for the WT and G22S channel respectively). Values are reported as mean ± SEM.

G. Example of a recorded ion current trace on a cortical neuron (18 DIV) expressing the G22S channel. The traces correspond to the recorded ion currents on the same neuron before (left dark blue trace) and after (right light blue trace) incubation with 1μM TTX. The enlarged insets illustrate a detail of the recoded traces reported in the respective upper panels. The enlarged insets show the recorded single eMscL channel currents (indicated by a green arrow) and the associated generation of neuronal action potential (indicated by a blue arrow) before the incubation with TTX. After treatment of the neuron with 1μM TTX, the enlarged inset shows the sole presence of the eMscL single channel ion currents.

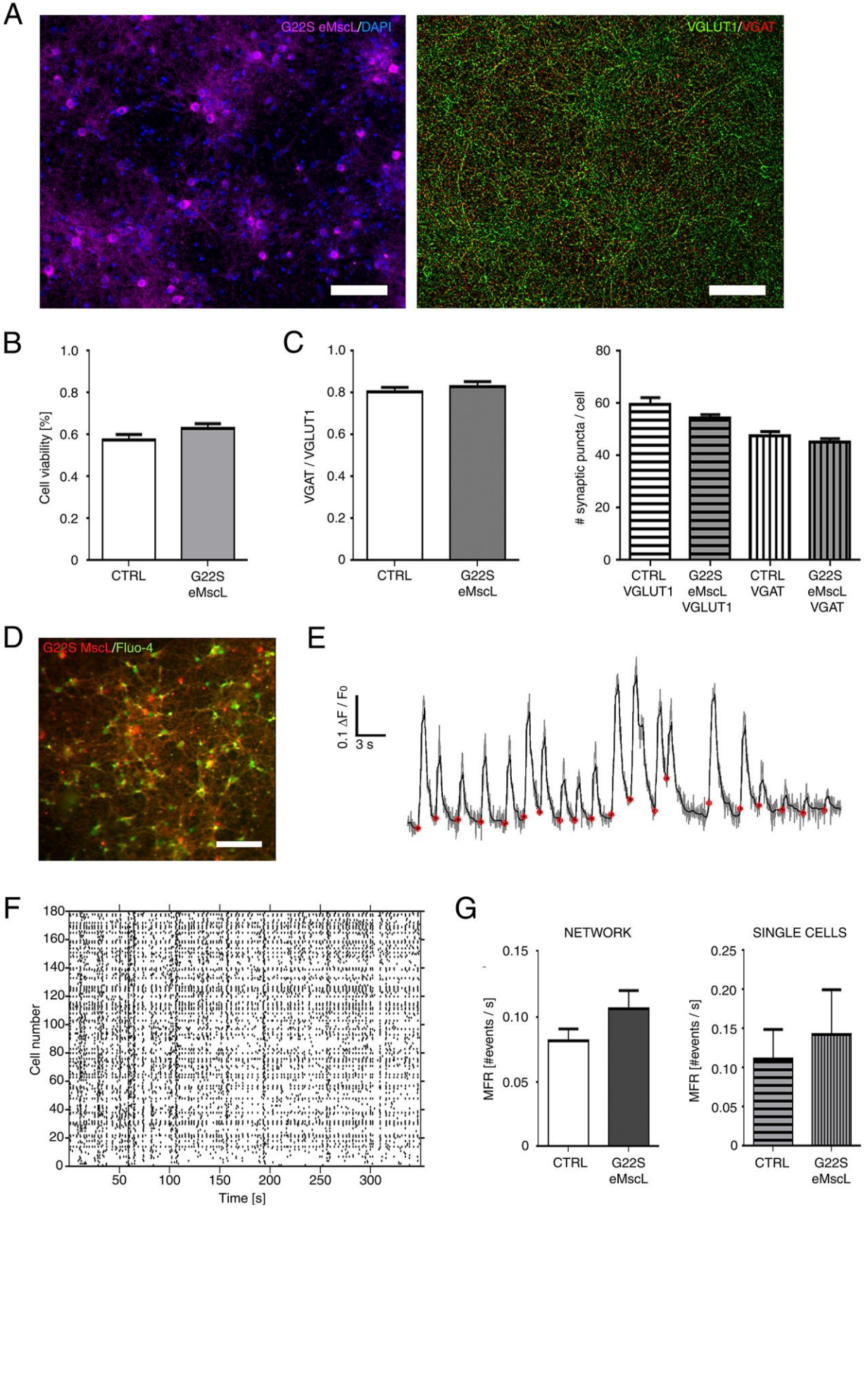

Fig. 4. Functional characterization of cortical neuronal networks expressing the G22S eMscL channel.

A. Fluorescence images of a cortical neuronal network (20 DIV) infected with the adeno-associated virus expressing G22S eMscL channel. On the left, the magenta color indicates the fluorescence signal of the tdTomato tagged to the eMscL channel and in blue the fluorescence of the DAPI nuclear staining. On the right, the fluorescence image of the excitatory and inhibitory synaptic puncta immuno-labeled with the VGLUT1 and VGAT markers (respectively in green and red color). Bars are 100 µm.

B. Bar plot of the percentage of viable cells of control cultures and cortical neuronal networks expressing the G22S channels (57%±3 and 63%±2 for the control and G22S neuronal networks respectively). Values are reported as mean ± SEM.

C. Bar plots reporting on the left, the ratio of VGAT/VGLUT1 synaptic puncta (0.81±0.02 and 0.83±0.03 for control and the eMscL expressing networks, respectively), and on the right, the number of VGAT and VGLUT1 synaptic puncta per cells. The average of synaptic puncta per cells were measured and normalized with respect to the average number of cells per field of view (for control network: VGAT= 47.60±1.70 and VGLUT1= 59.50±2.75 on 6 fields of view; for G22S expressing networks: VGAT= 64.32±19.25 and VGLUT1= 54.50±1.30 on 8 field of views). Values are reported as mean ± SEM.

D. Fluorescence image showing the field of view of a neuronal network expressing the G22S eMscL channel (in red), and the Fluo4-AM calcium indicator (in green). Bar is 100 µm.

E. Example of a single neuronal $\Delta F/F_0$ trace of a cortical network (20 DIV). The denoised trace is shown in black and superimposed on the raw trace (reported in gray color). The red dots indicate the automatically detected onset time of calcium fluctuation events (see methods section: Calcium imaging and data analysis).

F. Raster plot of the spontaneous calcium activity of single cells identified in the field of view of the neuronal network.

G. On the left, bar plots of the mean firing rate (MFR), expressed as number of events per second, of control and G22S eMscL expressing neuronal networks (n= 10 and 11, respectively). On the right, MFR plot of single cells expressing or not the G22S eMscL channel within the same neuronal networks (n= 1380 and 917 respectively). Values are reported as mean ± SEM.

Supplementary Figures

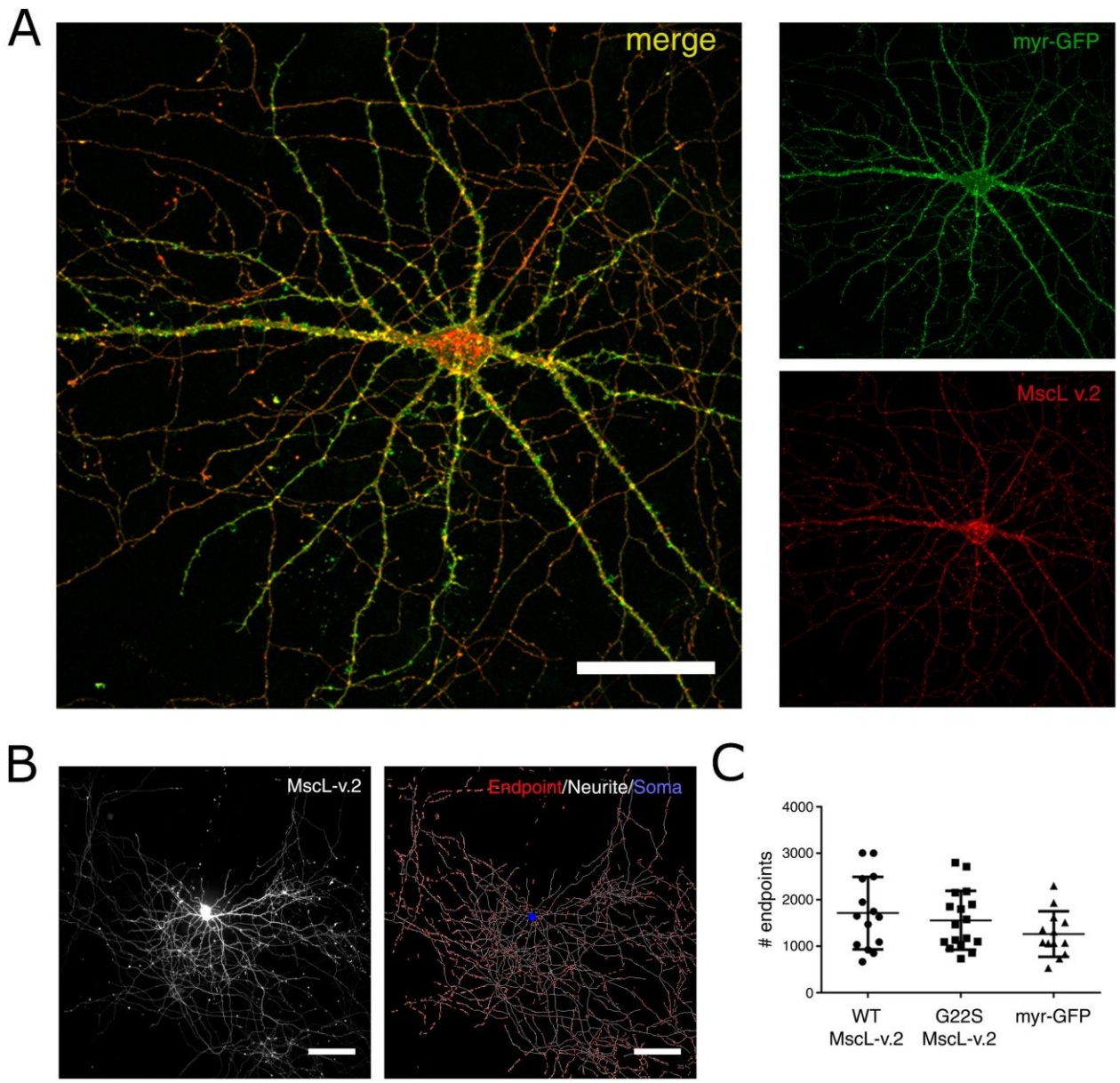

Fig. S1. Cortical neuron expressing the MscL-v.2

A. Cortical primary neuron (20 DIV) expressing the MscL-v.2 (red color), and the myristoylated GFP (green) constructs. The merge of the two fluorescence signals is shown in yellow. Scale bar= 50 μm.

B. On the left, the fluorescence image of a cortical neuron expressing the WT MscL-v.2 construct and, on the right, the detected skeleton of the same neuron is shown. The automatically detected endpoints, neurites, and cell soma are reported in red, white and blue color respectively.

C. Quantification of the number of endpoints detected on neurons expressing the two MscL constructs, and the myr-GFP construct (WT MscL-v.2: 1714±209 endpoints on 14 cells, G22S MscL-v.2: 1559±154 endpoints on 17 cells, myr-GFP: 1262±136 endpoints on 13 cells). Values are reported as mean ± SEM and no statistically significant differences are measured.

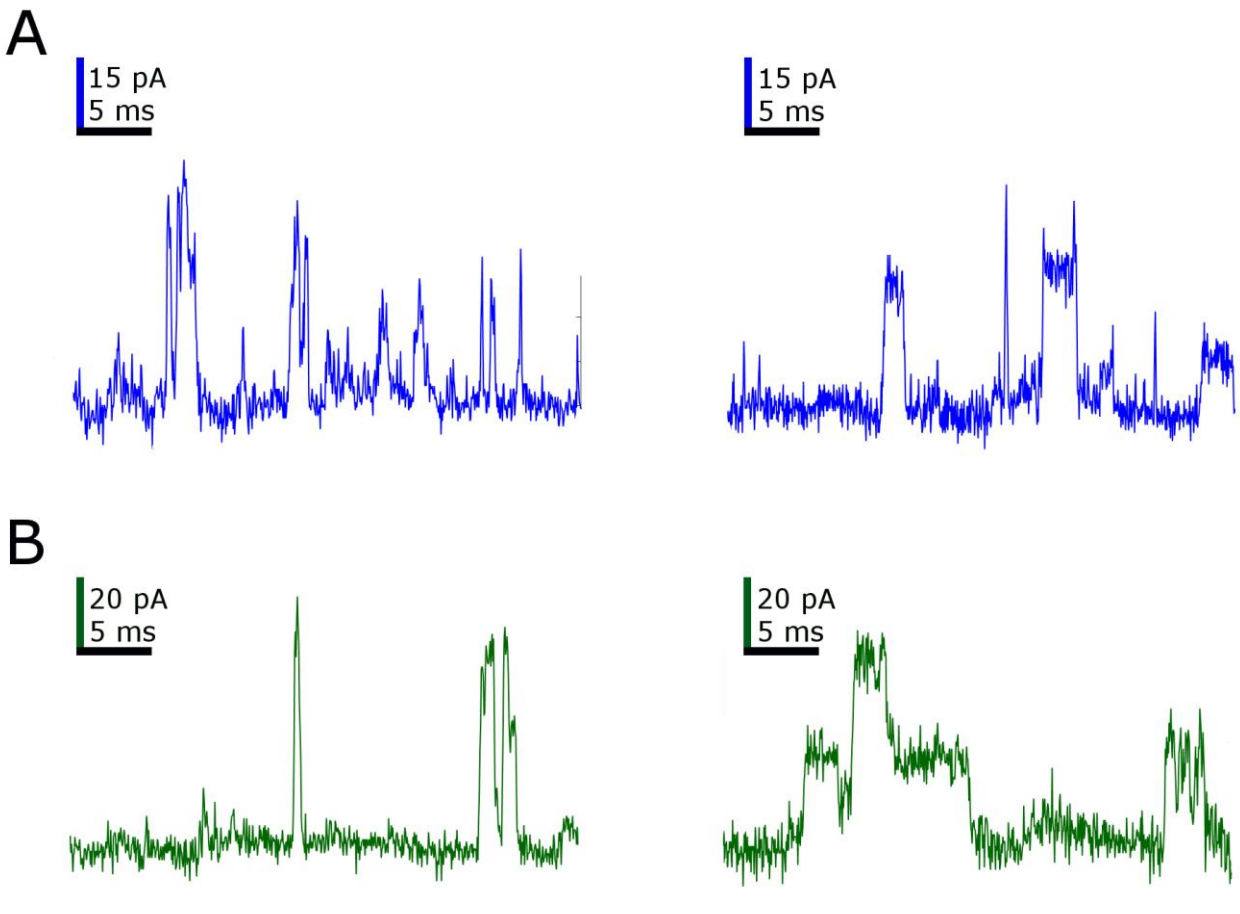

Fig. S2. Expanded view of the WT and G22S eMscL-induced currents in partial and full response.

A. Expanded view of a representative trace of partial response (left panel) and full response (right panel) recorded in WT eMscL expressing neurons in cell-attached configuration.

B. Expanded view of a representative trace of partial response (left panel) and full response (right panel) recorded in G22S eMscL expressing neurons in cell-attached configuration.

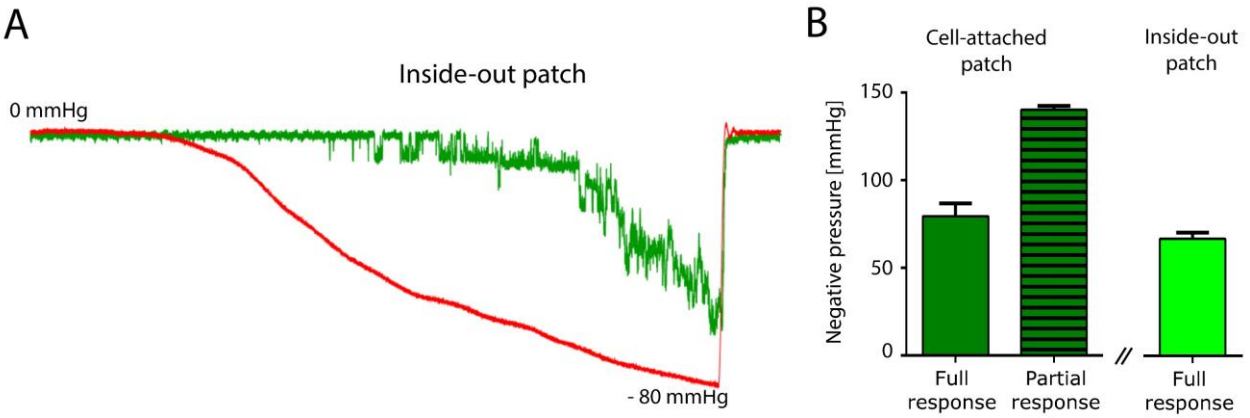

Fig. S3. Characterization of the activation pressure threshold of the virally encoded G22S eMscL construct.

A. Representative trace of the recorded full response (green trace) in excised patch-clamp experiment during the negative pressure stimulation (red trace).

B. Bar plots reporting the quantification of the pressure activation thresholds at which the partial (141±0.48 mmHg, N= 65 stimulation trials) and full (70±0.72 mmHg, N= 21 stimulation trials) current response in cell-attached configuration (green plots), and in excised patch (67±0.14 mmHg, N= 69 stimulation trials) configuration (light green) occur. Values are reported as mean ± SEM.

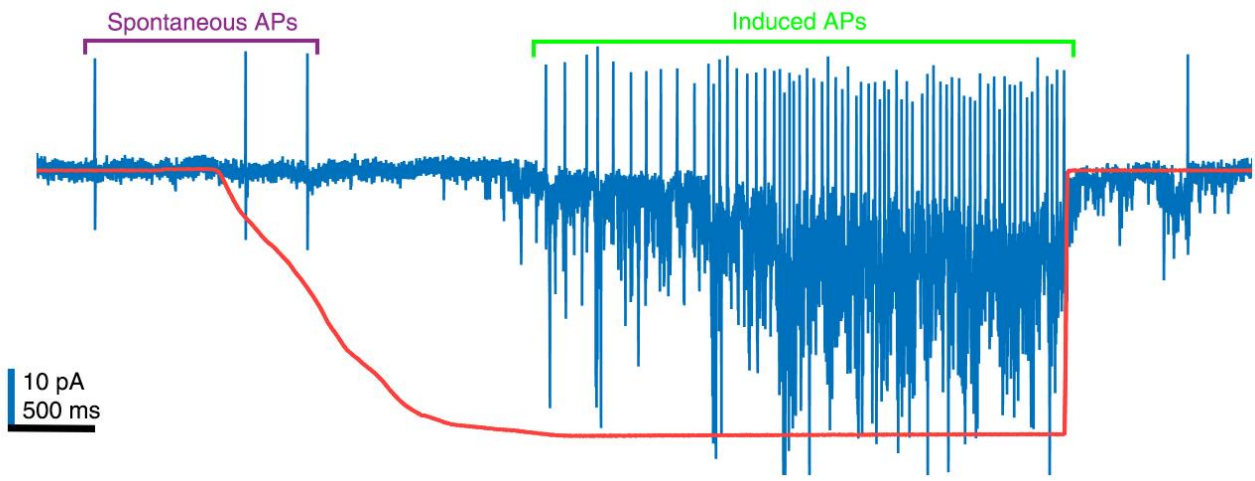

Fig. S4. Mechanical stimulation of neuron expressing the G22S eMscL channel increases its firing rate.

Trace of the recorded ion currents (blue trace) during negative pressure stimulation (red trace) of the membrane patch, in a neuron (18 DIV) expressing the G22S eMscL channel. Violet and green lines respectively highlight the spontaneous and induced APs.